Available online at www.sciencedirect.com
SCIENCE DIRECT®
Journal of Petroleum Science and Engineering 46 (2005) 121–137
JOURNAL OF PETROLEUM SCIENCE & ENGINEERING
www.elsevier.com/locate/petrol

Pore space reconstruction using multiple-point statistics

Hiroshi Okabe[a,b,*], Martin J. Blunt[a]

[a]Department of Earth Science and Engineering, Imperial College London, SW7 2AZ, UK
[b]Japan National Oil Corporation, 2-2-2 Uchisaiwai-cho, Chiyoda-ku 100-8511, Japan

Received 11 August 2003; accepted 25 August 2004

Abstract

The reconstruction of porous media is of great interest in a wide variety of fields, including earth science and engineering, biology, and medicine. To predict multiphase flow through geologically realistic porous media it is necessary to have a three-dimensional (3D) representation of the pore space. Multiple-point statistics were used, based on two-dimensional (2D) thin-sections as training images, to generate 3D pore space representations. The method was borrowed from geostatistical techniques that use pixel-based representations to reproduce large-scale patterns. Thin-section images can provide multiple-point statistics, which describe the statistical relation between multiple spatial locations. Assuming that the medium is isotropic, a 3D image can be generated that preserves typical patterns of the void space seen in the thin sections. The method is tested on Fontainebleau and Berea sandstones for which 3D images from micro-CT scanning are available. The use of multiple-point statistics predicts long-range connectivity of the structures (measured by local percolation probability) better than standard two-point statistics methods. The selection of multiple-point statistics is a key issue and is discussed in detail.

Keywords: Pore space representation; Multiple-point statistics; Reconstruction; Long-range connectivity; Percolation probability

1. Introduction

Transport properties such as relative permeability and capillary pressure functions define the flow behavior of porous media. These functions critically depend on the geometry and topology of the pore space, the physical relationship between rock grains and the fluids, and the conditions imposed by the flow process. A quantitative prediction of petrophysical properties in disordered media, such as sedimentary rock, frequently employs representative microscopic models of the microstructure as input. Pore structural information must be available in order to predict fluid flow properties using network models (Blunt et al., 2002) or other approaches, such as the lattice-Boltzmann method (Chen and Doolen, 1998).

The numerical reconstruction of 3D materials, such as porous and composite media, has various potential

* Corresponding author. Present address: Oil and Gas Technology Research and Development, Japan Oil, Gas and Metals National Corp., 1-2-2 Hamada, Mihama-ku, Chiba 261-0025, Japan. Tel.: +81 43 276 9263; fax: +81 43 276 4063.
E-mail address: okabe-hiroshi@jogmec.go.jp (H. Okabe).

0920-4105/$ - see front matter © 2004 Elsevier B.V. All rights reserved.
doi:10.1016/j.petrol.2004.08.002

applications in earth science and engineering, biology, and medicine. Effective reconstruction methods allow generation of realistic structures and subsequent analyses can be performed on the images to compute macroscopic parameters, such as transport and mechanical properties.

Several methods have been proposed to generate 3D pore space images. A series of 2D sections can be combined to form a 3D image. This is a laborious operation limited by the impossibility of preparing cross sections with a spacing of less than about 10 μm (Dullien, 1992). However, recent advances, such as the use of a focused ion beam (Tomutsa and Radmilovic, 2003) allow higher resolution images (sub-micron size) to be constructed. Another approach is to use non-destructive X-ray computed micro-tomography (Dunsmuir et al., 1991; Spanne et al., 1994; Coles et al., 1998) to image a 3D pore space directly at resolutions of around a micron. However, this resolution is not sufficient to image the sub-micron size pores that are abundant in carbonates, which can be imaged by 2D techniques such as scanning electron microscopy (SEM). The sub-micron structures of real rocks have been studied using laser scanning confocal microscopy (Fredrich, 1999). It has, however, limited ability to penetrate solid materials. In the absence of higher resolution 3D images, reconstructions from readily available 2D microscopic images are the only viable alternative.

2D high-resolution images provide important geometrical properties such as the porosity and typical pore patterns. Based on the information extracted from 2D images, one promising way is to reconstruct the porous medium by modeling the geological process by which it was made (Bryant and Blunt, 1992; Bakke and Øren, 1997; Pilotti, 2000). Although the process-based reconstruction is general and it is possible to reproduce the long-range connectivity, there are many systems for which the process-based reconstruction is very difficult to apply. For example, for many carbonates it would be very complex to use a process-based method that mimics the geological history involving the sedimentation of irregular shapes followed by significant compaction, dissolution and reaction (Lucia, 1999). In these cases it is necessary to find another approach to generate a pore space representation. One method is to use statistical techniques to produce a 3D image from 2D image analysis (Quiblier, 1984; Adler et al., 1990, 1992). Traditionally porosity and two-point statistics have been used to achieve this. These methods have been extended to include other geometrical properties to improve the quality of the reconstructed images (Roberts, 1997; Roberts and Torquato, 1999; Yeong and Torquato, 1998a,b; Manwart et al., 2000; Talukdar et al., 2002). These images, however, often fail to reproduce the long-range connectivity of the pore space, especially for low porosity materials and particulate media, such as grain or sphere packs because of the low-order information used (Hazlett, 1995, 1997; Coles et al., 1998; Levitz, 1998; Biswal et al., 1999; Kainourgiakis et al., 2000; Øren and Bakke, 2002, 2003).

A multiple-point statistics technique first introduced in geostatistics to represent connected geological bodies, such as sand channels, at the field scale is used to reconstruct pore space images (Caers, 2001; Strebelle et al., 2003). Conceptually the problem is similar: pore spaces that have a high degree of interconnectivity must be generated. A key aspect is the proper selection of the multiple-point statistics to reproduce satisfactory images. Fontainebleau and Berea sandstone are used as test cases because they have been characterized thoroughly by other means. Fig. 1 shows an image of Fontainebleau

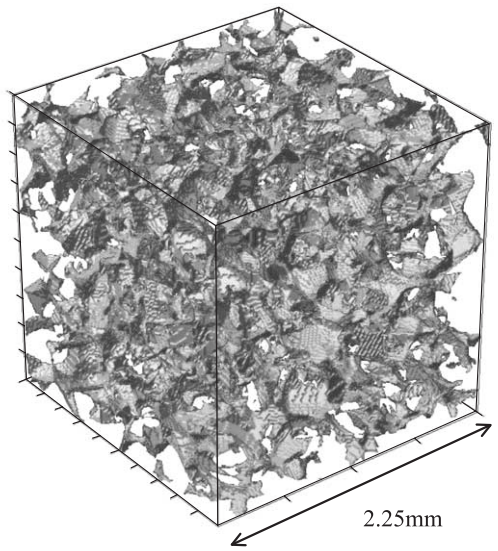

Fig. 1. A 3D pore space representation of Fontainebleau sandstone. The pore space is shown in gray. This image was generated using micro-CT scanning with a resolution of 7.5 μm.

sandstone obtained by micro-CT scanning (Dunsmuir et al., 1991).

2. Methodology

2.1. Multiple-point statistics method

Multiple-point statistics method requires a densely and regularly sampled training image describing the geometries expected to be exist in the real structure (Caers, 2001; Strebelle et al., 2003). For example, photographs of outcrops at the field scale and microscope images at the pore scale can be used as training images.

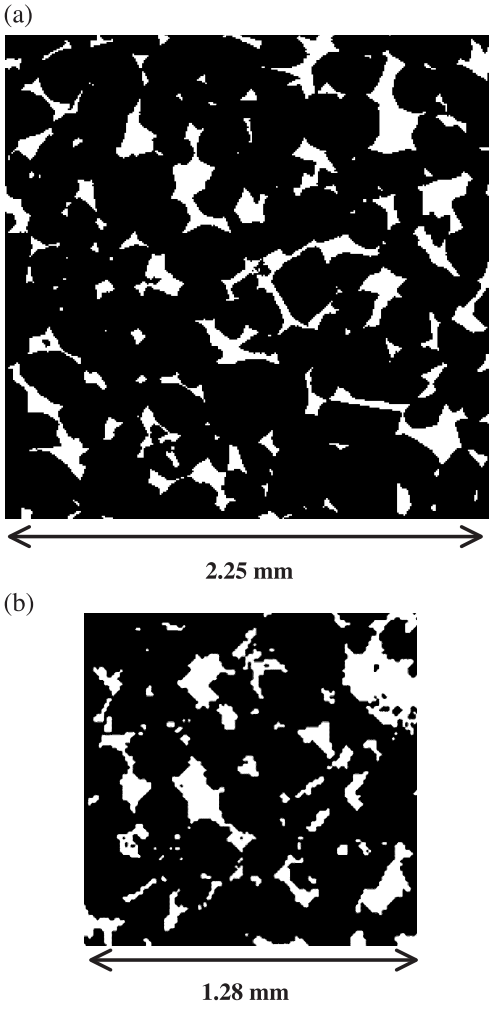

Fig. 2. Thin-sections as training images taken from 3D micro-CT images. The pore space is shown white and the grain black. (a) Fontainebleau sandstone with a porosity, ϕ=0.1364 (300^2 pixels). (b) Berea sandstone with ϕ=0.1773 (128^2 pixels). The resolutions of the images are 7.5 and 10 μm, respectively.

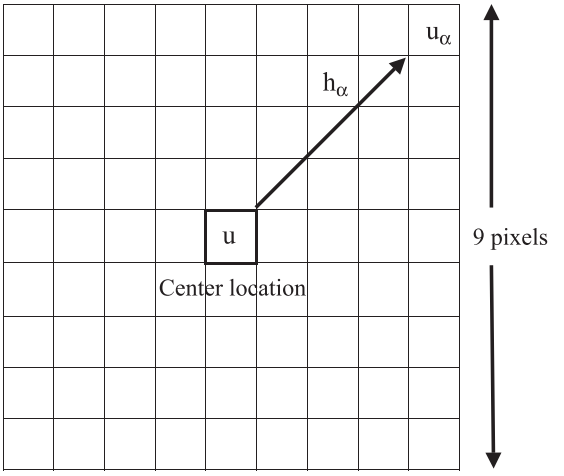

Fig. 3. A 9×9 template to capture multiple-point statistics. The training image is scanned and each occurrence of any possible pattern of void space and grain is recorded.

2.1.1. Borrowing multiple-point statistics from training images

The training image of Fig. 2 (thin-section image) is scanned using a *template* t composed of n_t locations $\mathbf{u}_\alpha$ and a central location $\mathbf{u}$:

$$\mathbf{u}_\alpha = \mathbf{u} + \mathbf{h}_\alpha \qquad \alpha = 1,..,n_t \tag{1}$$

where the $\mathbf{h}_\alpha$ are the vectors describing the template. For example, in Fig. 3, $\mathbf{h}_\alpha$ are the 80 vectors of the square 9×9 template. The template is used to scan the training image and collect the data event at each location $\mathbf{u}$. The data event (or the pattern), for example shown in Fig. 4, is defined by

$$dev(\mathbf{u}) = \{i(\mathbf{u}); i(\mathbf{u}+\mathbf{h}_\alpha), \quad \alpha = 1,..,n_t\} \tag{2}$$

where $i(\mathbf{u})$ is the data value at the point within the template. Each point in the template has a number to identify the pattern and to store the pattern in the memory. The set of all data events scanned from the training image results in a *training data set*

$$Set = \{dev(\mathbf{u}_j), \quad j = 1,..,N_t\} \tag{3}$$

where Set refers to the training data set constructed with template t. N_t is the number of different central

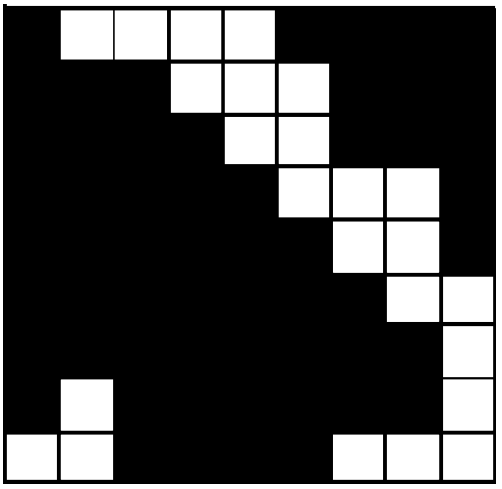

Fig. 4. A data event (or a pattern) measured by 9×9 template. The frequency of every possible data event is found by scanning the template (Fig. 3) over the training image.

locations of template t over the training image. The selection of the template geometry is important and various template sizes n_t should be tried in order to reproduce better structures.

2.1.2. Pattern reproduction

To reconstruct pore scale structures, binarized thin section images were used as training images that have only void or solid. A detailed discussion of the training image is presented later under Rock Sample.

The probability of occurrence of any data event dev_n associated with the data template t can be inferred from the training image by counting the number $c(\mathrm{dev}_n)$ of replicates of dev_n found in the training image. A replicate should have the same geometry and the same data values as dev_n. The multiple-point statistics can be identified to the proportion: $\Pr(\mathrm{dev}_n) \approx c(\mathrm{dev}_n)/N_n$ where N_n is the size of the training image. The key to this algorithm is the determination of local conditional probability distribution functions (cpdf). The probability that the unknown attribute value $i(\mathbf{u})$ takes any of two possible states (void or solid) given n nearest data during the reproduction at any unsampled location $\mathbf{u}$ must be evaluated. If multiple-point statistics are available, then the conditioning of $i(\mathbf{u})$ to the single global data event dev_n can be considered, and the conditional probability can be identified to the training proportion. The cpdf is inferred directly and consistently from the training image. The multiple-point statistics, the geometrical structures in other words, are borrowed directly from the training image.

This approach can theoretically apply to a 3D field when 3D structural information is available. Since it is difficult or impossible to measure 3D sub-micron scale data, our only alternative is to use 2D images to measure multiple-point statistics. In order to generate 3D structure from 2D information, measured multiple-point statistics on one plane are rotated 90° around each principal axis. In other words, measured statistics on the *XY* plane are transformed to the *XZ* and the *YZ* planes with an assumption of isotropy in orthogonal directions. At every voxel in order to assign void or solid phase, three principal orthogonal planes, *XY*, *XZ* and *YZ* intersecting this voxel are used to find conditioning data on these planes one by one. Each probability of the phase at this voxel on the different planes are estimated by this process, and then the three measured probabilities are weighted by the number of conditioning data on each plane to obtain a single probability on this voxel. Finally, the phase at the voxel is assigned based on this weighted probability to generate a 3D image. There is less conditioning data during the initial stage of the reproduction. In this case, the porosity value can be used as the probability.

To borrow directly all required cpdf from a training image possibly leads to having excessive amounts of information. In a designated template t of n data variables, inference of a probability distribution function conditional to a data event dev_n requires that enough occurrences, which are dependent on the size of the training image, should be found. Each of the 80 nodes in the data template (9×9 square shape), except a center point, can take two states (void or solid). This leads to 2^{80} possible data events which means that a relatively small number of cpdf can be actually inferred from the training image. To alleviate this problem, at each unsampled node, infer the local cpdf by scanning the training image with progressive reduction of the size n of the conditioning data event dev_n until a designated minimum number of replicates of dev_n are found. To minimize the repetitive process and the calculation time, each unsampled grid node is visited only once using a random path and each simulated value becomes a conditioning datum value. Needless to say, conditioning data are frozen at their

data location and are used for the successive simulation. These cycles are iterated until all the grids are simulated. In order to avoid the repetitive scanning of the training image and to store multiple-point statistics effectively, a dynamic data structure called a *search tree* is used to store all training cpdf in advance. The algorithm is explained by a flow chart in Fig. 5.

In the presence of large-scale structures, the use of a single limited size template would not suffice to model the large-scale characteristics observed in the training image of Fig. 6. In this figure, both a small template and a template large enough to capture the large-scale structures are applied to the thin section image. Thus, a large template is necessary to reproduce large-scale structures observed in the train-

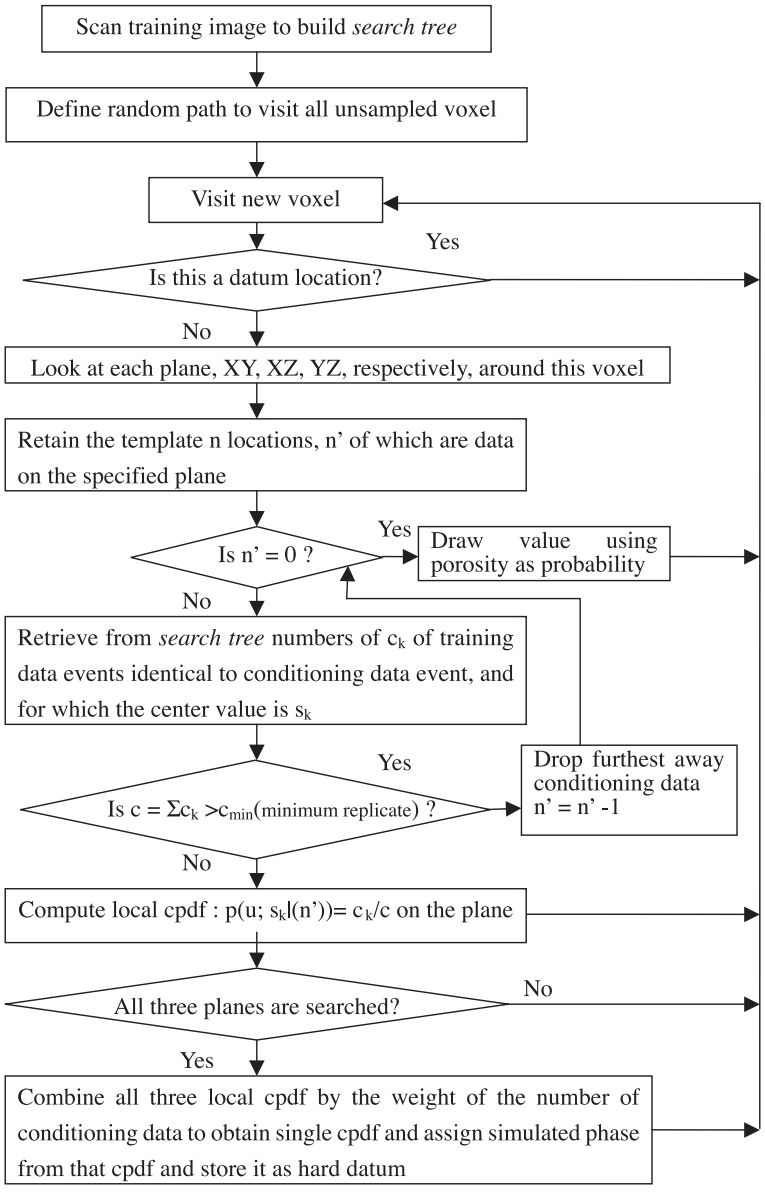

Fig. 5. Flow diagram of multiple-point statistics reconstruction of pore space images.

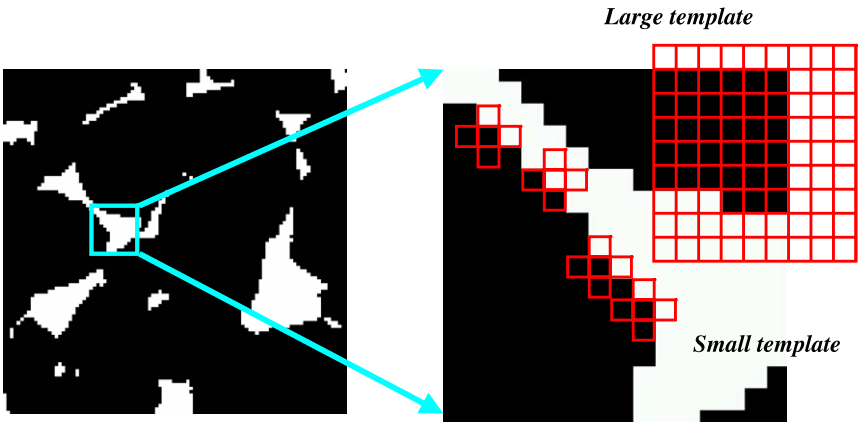

Fig. 6. A small template and a template large enough to capture pore-scale structures.

ing image. The template size can be theoretically expanded to match the largest structure in the training image; however, the template size is limited by memory limitations in the numerical simulation. Although the numerical modeling is always limited at certain points, an alternative approach can be introduced by a sort of multigrid simulation (Caers, 2001; Strebelle et al., 2003). Four different sized templates (Fig. 7) are used to scan the training image, resulting in four different data sets Set_{t1}, Set_{t2}, Set_{t3} and Set_{t4}. Larger scale templates can simply be expanded from the small-scale template. In a multigrid system, a simulation is first performed on the coarsest grid. Once the coarse simulation is finished, the simulated values are assigned to the correct grid locations on the finer grid, and are used as conditioning data on the finer grid. When large-scale structures exist in the training image, this multigrid approach is effective to measure the large-scale multiple-point statistics while requiring relatively little memory (Caers, 2001; Strebelle et al., 2003).

2.2. Image processing-noise reduction and smoothing

There is noise in 3D images generated from 2D data, due to insufficient statistics, which is inevitable when stochastic methods are used. This unrealistic noise in the image can be reduced by image processing. Some researchers (Ioannidis et al., 1997; Liang et al., 1998) who use stochastic

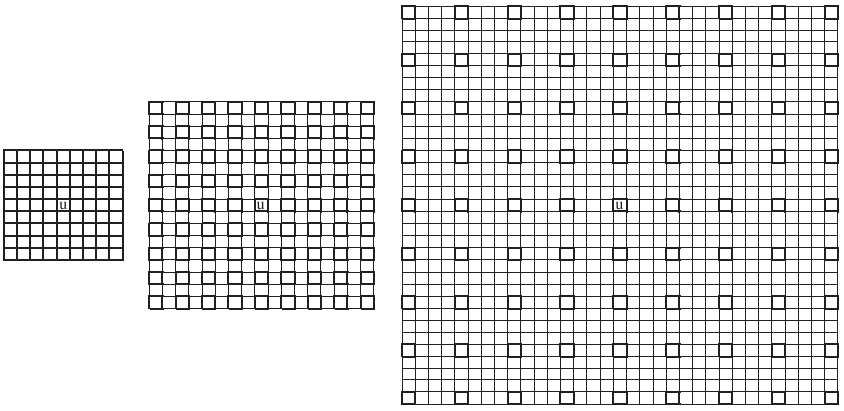

Fig. 7. Expanded templates to capture large-scale structure (from left to right). A form of multigrid simulation is performed with an image first generated using the largest template and then successively smaller templates are used where the large-scale information acts as conditioning data.

reconstruction have taken noise canceling as a post-processing step. For example, Liang et al. (1998) measured the fractions of non-percolating solid and void phases as 0.0008 and 0.012, respectively, in their reconstructed structures. The non-percolating solid phases correspond to islands isolated inside the void phase. Since this is impossible in real porous media they were changed to appear as void phase. The same process was used for noise canceling. This process may slightly increase the porosity of the reconstructed structure; however, Liang et al. confirmed the effect of changing structure was negligible by comparing the normalized two-point correlation function in the reference and the reconstruction. Only a very small fraction of isolated solid phase (around 0.0001) was changed to the void phase. In addition to this process, simple binary image processing to reduce noise in the void phase and smooth the boundary between void and solid is used. First a 3D opening operation (combination of dilation and erosion processes) is used in a $3\times3\times3$ cubic neighborhood pattern containing a total of 27 pixels (Serra, 1992). Although more effective operations can be explored for the simulated pore space representation, it has been confirmed this simple operation reasonably smoothes the 3D image and reduce the noise, as shown in Results. After opening operation the image has a higher porosity than the original. We adjust the porosity by counting the number of neighbor pixels of the opposite phase in a $3\times3\times3$ region and compare this number to some threshold value (coefficient value). The phase of the central pixel is changed if the count is exceeded (Russ, 1994). Classical erosion or dilation is this operation using a coefficient of zero. The coefficient value is chosen to result in the correct, original, value of porosity.

3. Rock sample

3.1. Fontainebleau sandstone

A 3D non-destructive X-ray microtomographic image of Fontainebleau sandstone, Fig. 1, is used as the experimental reference data and parts of training images for our method (Dunsmuir et al., 1991; Lindquist et al., 2000). This sandstone serves as a basis for many rock physics experiments because of its simplicity (Bourbie et al., 1987). Fontainebleau sandstone consists of monocrystalline quartz grains that have been well rounded through transport for long periods before being deposited. The sample used had well sorted grains of around 200 μm in diameter. The sand was cemented by silica crystallizing around the grains (quartz overgrowths). Fontainebleau sandstone exhibits intergranular porosity ranging from 0.03 to roughly 0.3 depending on the degree of compaction and diagenesis.

The porosity of our microtomographic image is 0.1355 compared to 0.1484 of the larger original core which has a permeability of 1.3D and a formation factor of 22.1. The difference between the porosity of the original core and that of the microtomographic data is due to the heterogeneity of the sandstone, the difference in sample size and resolution of microtomography. The experimental sample is referred to as micro-CT in the following. A 2D cut of pore space of the experimental sample is shown in Fig. 2(a).

3.2. Berea sandstone

The Berea sandstone is another rock standard that has been widely used for laboratory experiments (Dullien, 1992). It contains minor amounts of feldspar, dolomite, and clays. The sandstone also occurs in the oil and gas producing formation in the Michigan Basin. This particular Berea sandstone sample with clays has a porosity of 0.1775 in the tomographic image compared to 0.23 of the larger original core which has a permeability of 1.1D (Hazlett, 1995). The differences between the porosity of the original core and that of the microtomographic data are again due to the heterogeneity of the sandstone, the difference in sample size and the resolution of the microtomography. A 2D slice of the micro-CT image was shown in Fig. 2(b).

3.3. Selection of a 2D thin-section

Fig. 2 shows 2D binary images of 2D thin section cuts from the 3D microstructures of the sandstone samples. The porosity measured from a certain 2D plane fluctuates slice by slice as shown in Fig. 8. In order to reconstruct a 3D structure effectively from a 2D cut, a representative 2D image should be selected

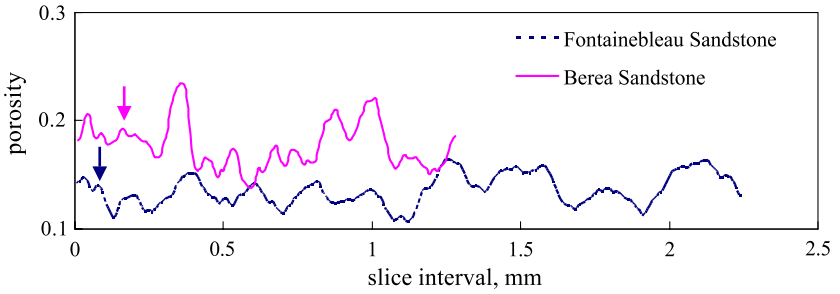

Fig. 8. Porosity fluctuation before and after post-processing for an unconditional reconstruction of Fontainebleau sandstone (ϕ=0.1355) compared with the micro-CT image of Fontainebleau sandstone.

in terms of porosity. The slices indicated in Fig. 8 by arrows are used.

4. Results

4.1. Template selection

This method has more flexibility than the traditional two-point correlation method because the template used to generate multiple-point statistics as well as the training image can be changed. A key aspect is the proper selection of multiple-point statistics to produce satisfactory images. Four different sized templates are used with same 9×9 square shape, spanning 9×9, 18×18, 36×36 and 72×72 pixels (Fig. 7). A larger template can capture large structures; however, it takes much more CPU time and introduces more noise if the training image does not provide sufficient statistics. For example, if the square templates were expanded from 9×9 to 11×11 with same four-stage multigrid system, the CPU time approximately doubled for a 200^3 structure and the images became slightly noisier. A smaller template leads to a reconstruction with fewer constraints and less noise, but large structures are not so accurately reproduced. Thus a 9×9 template, after considering larger and smaller templates, gave the optimum combination of CPU time, lack of noise and preservation of large features in the pore space.

Fig. 9 shows a 2D multiple-point reconstruction of the Fontainebleau sandstone without conditioning data. An image of 200×200 pixels corresponding to 1.5×1.5 mm was generated using a single template (Fig. 3, a 9×9 square template) and is shown in Fig. 9(a). Fig. 9(b) shows an image generated using the four-stage multigrid system shown in Fig. 7. Notice that this improves the quality of the image and can

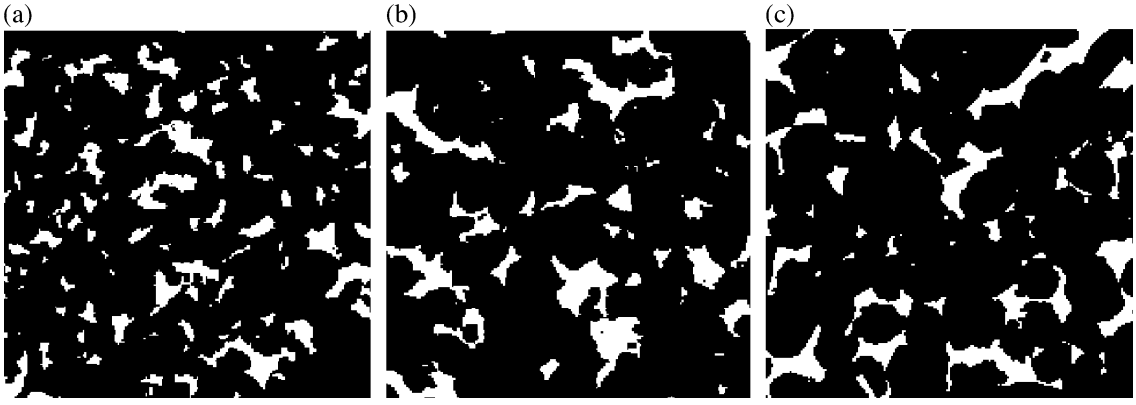

Fig. 9. Comparison of different 2D images. All the images are comprised of 200×200 pixels. (a) A statistically generated image (ϕ=0.1367) using a single small-scale template. (b) An improved image (ϕ=0.1354) using the multigrid templates shown in Fig. 7. (c) A reference image (ϕ=0.1376) from micro-CT data.

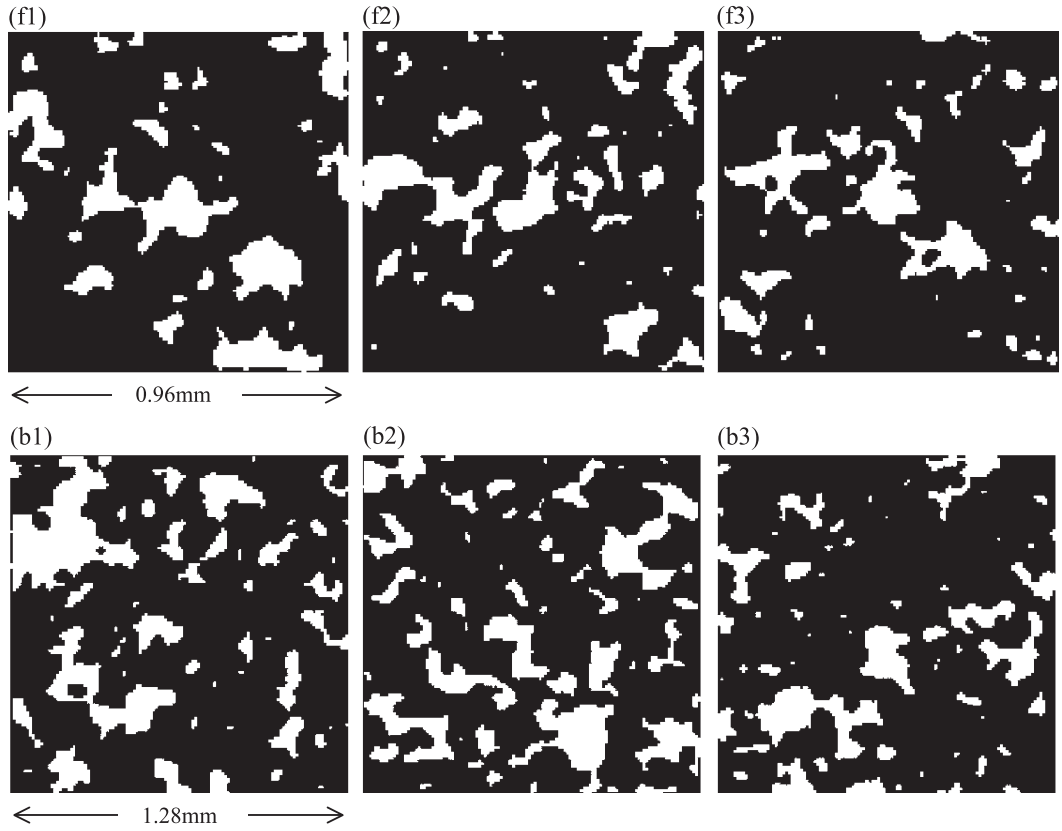

Fig. 10. 2D cuts through unconditional 3D reconstructions of sandstones (128^3 pixels,) with the slice porosities, ϕ indicated. The images are post-processed. (f1) *XY* plane (*Z*=64, ϕ=0.1688), (f2) *XZ* plane (*Y*=64, ϕ=0.1492), (f3) *YZ* plane (*X*=64, ϕ=0.1325) for Fontainebleau sandstone (7.5 μm/pixel) with a four-stage multigrid approach. (b1) *XY* plane (*Z*=64, ϕ=0.2051), (b2) *XZ* plane (*Y*=64, ϕ=0.2045), (b3) *YZ* plane (*X*=64, ϕ=0.1541) for Berea sandstone (10 μm/pixel). A two-stage multigrid approach is applied for Berea sandstone because the training image is small (128^2) and has insufficient statistics for a four-stage multigrid approach.

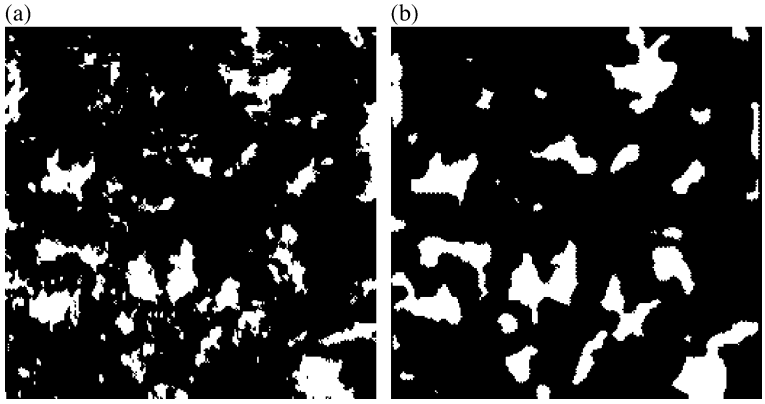

Fig. 11. 2D image comparison between (a) the original image (ϕ=0.1519) and (b) smoothed image (ϕ=0.1518) after post-processing for the unconditional 3D reconstruction of Fontainebleau sandstone.

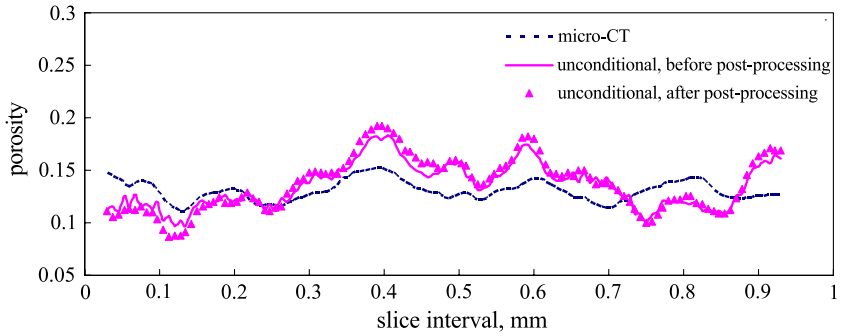

Fig. 12. Porosity fluctuations in the reconstructed structure (before and after post-processing). Notice that the porosity fluctuations are similar in magnitude to those in the reference image.

reproduce typical pore shapes accurately. In 2D, visual inspection of this figure reveals that the simulated structure using a multigrid process closely resembles the experimental microstructure shown in Fig. 9 even though there was no conditioning data and no post-processing of the image.

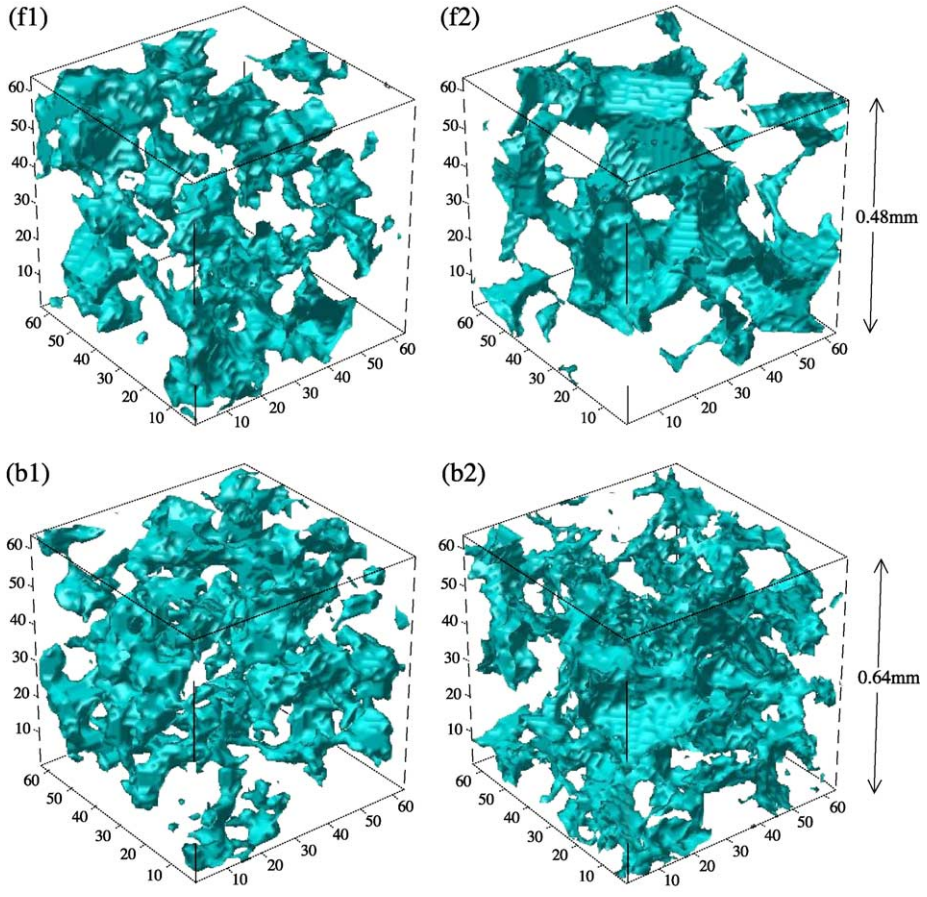

Fig. 13. Subgrids of 3D reconstructed images. (f1) A reconstructed Fontainebleau sandstone, ϕ=0.1380 compared with (f2) the micro-CT image, ϕ=0.1379. (b1) A reconstructed Berea sandstone, ϕ=0.1747 compared with (b2) the micro-CT image, ϕ=0.1781. Notice that the porosity in the original reconstructed image is same as that of larger micro-CT image.

4.2. Unconditional 3D reconstruction

Two-dimensional reproduction from 2D multiple-point statistics is not challenging because sufficient statistics are measured on a 2D training plane. Generating a 3D structure from 2D information is a truly challenging task. The training images shown in Fig. 2 and the templates in Fig. 7 were used and the multiple-point statistics in a 2D plane were rotated by 90° around the principal axes in order to generate a 3D structure as explained in Fig. 5.

Fig. 10 shows 2D cuts of 3D reconstructions without conditioning data. A four-stage multigrid approach is applied to Fontainebleau sandstone, but only a two-stage multigrid approach is used for Berea sandstone because the training image taken from the micro-CT scanning is too small (128^2 pixels) to give reasonable statistics for larger template. There is noise in the reconstructed structures, which is not observed in the training image. However, characteristic shapes of void and solid are reasonably reconstructed. In order to suppress unrealistic noise and smooth the image, post-processing was applied as described in the Methodology. The opening operation was used, and then additional erosion with the coefficient of 9–12 was taken in order to adjust the porosity value. Images between original reconstructed images and smoothed images after post-processing are compared in Fig. 11. The noise is significantly reduced and characteristic structures of the void space are reasonably preserved after the processing. The porosity of each plane is decreased or increased slightly; however, it is not drastically changed, as shown in Fig. 12.

3D reconstructed rocks are visually compared in Fig. 13. The pore space of reconstructed Fontainebleau sandstone is more poorly connected than that of the micro-CT image. The pore surface of this low

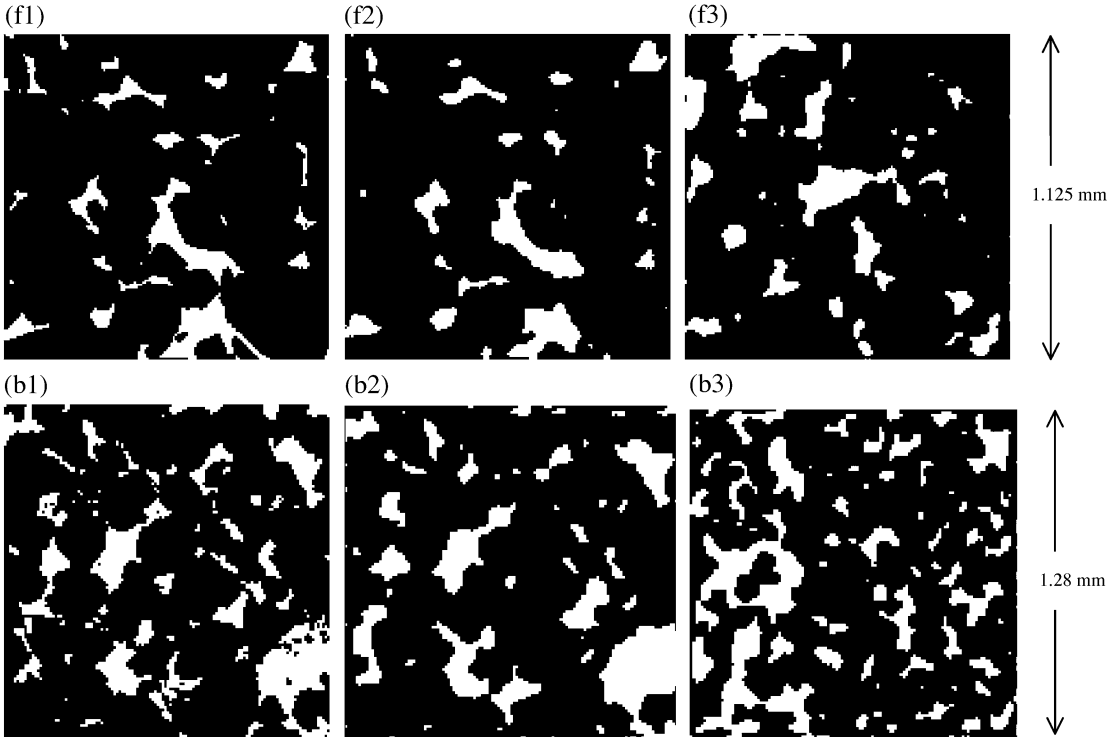

Fig. 14. 2D cuts through conditional 3D reconstructions of sandstones after post-processing. (f1) *XY* plane (Z=75, conditioning data, ϕ=0.1016), (f2) *XY* nearest conditioning plane (Z=74, ϕ=0.0973), (f3) *YZ* plane (X=75, ϕ=0.1252) for Fontainebleau sandstone (150^3, 7.5 μm/pixel). (b1) *XY* plane (Z=64, conditioning data, ϕ=0.1773). (b2) *XY* nearest conditioning plane (Z=65, ϕ=0.1942). (b3) *XZ* plane (Y=64, ϕ=0.2175) for Berea sandstone (128^3, 10 μm/pixel).

porosity rock is not well reproduced by the method and its pore space is much rougher than that of the micro-CT image. As this Fontainebleau sandstone has a characteristic structure, an object-based method, such as the geological process modeling described before, is better able to reproduce this kind of rock. On the other hand, the reconstructed image of Berea sandstone is relatively well reproduced.

4.3. Conditional 3D reconstruction

A part of the training image also can be used as conditioning data to generate a more realistic structure. Since more information is incorporated, a better reconstruction can be made. However, it is not always necessary because the amount of conditioning data from the training image is limited. For example, when a 150^3 structure is generated with one plane as a constraint, the ratio of the number of conditioning data over that of total data points in the structure is 1/150, too small to make a significant difference to the quality of the final image. However, the constraints affect the reconstruction in the region near the conditioning data. Fig. 14 shows 2D cuts of conditional reconstruction after post-processing. This reconstruction took 12 h CPU time with an Intel Xeon 1.7 GHz computer. Part of the 2D training image was used as conditioning data. It is evident from the figure that near the conditioning data the quality of the image is good, and that typical pore shapes are more poorly reproduced away from the conditioning plane or in orthogonal directions. Isotropy is assumed in our reconstruction; however, more conditioning data, such as several thin section images, can be used as constraints and multi-orientation thin section images can provide more statistics when significant anisotropy is expected.

4.4. Autocorrelation function and specific surface area

The void–void autocorrelation function of the 3D microstructure is used in traditional two-point

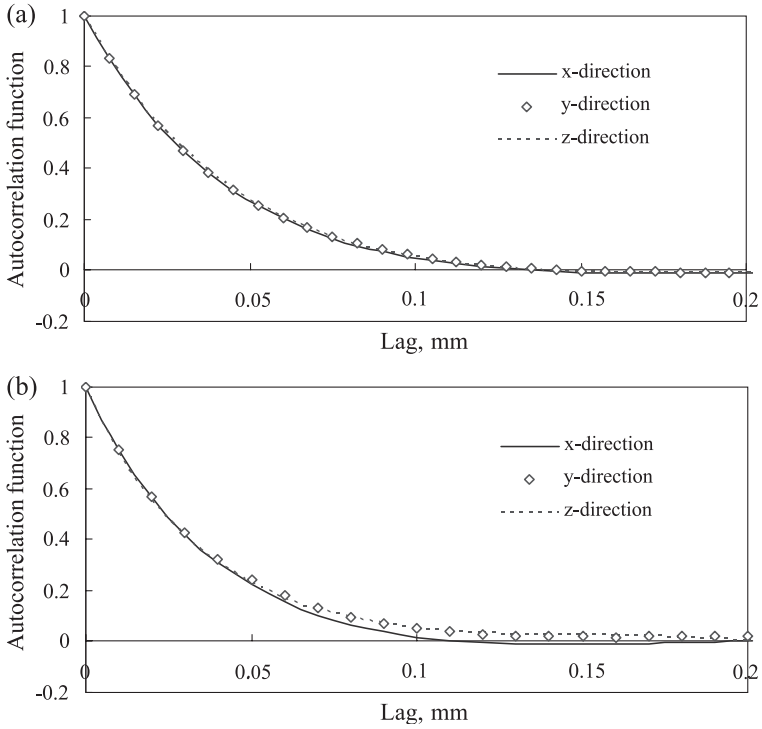

Fig. 15. Void–void autocorrelation function of the reference structure defined by Eq. (5) measured in three orthogonal directions. (a) Fontainebleau sandstone. (b) Berea sandstone.

statistical reconstruction as one of the matching parameters. When the microstructure is defined by the binary phase function ($Z(\vec{r}) = 1$ if $\vec{r}$ belongs to void space, $Z(\vec{r}) = 0$ otherwise), the void–void autocorrelation function $R_Z(\vec{u})$ is defined by

$$\phi = \overline{Z(\vec{r})} \tag{4}$$

$$R_Z(\vec{u}) = \frac{\overline{[Z(\vec{r}) - \phi][Z(\vec{r} + \vec{u}) - \phi]}}{[\phi - \phi^2]} \tag{5}$$

where overbars denote statistical averages and $\vec{u}$ is a lag vector. Fig. 15 shows the autocorrelation functions for the reference images measured in three orthogonal directions. The autocorrelation functions are virtually identical in the three directions, verifying our assumption of isotropy. Fig. 16 shows the autocorrelation functions averaged over three orthogonal directions compared to those measured on the reconstructed images and on the training images. The agreement is excellent, especially to those of the training images, demonstrating that the multiple-point statistics method does preserve two-point statistics adequately.

When the reconstruction has the same correlation function as the microstructure measured by micro-CT, both digitized 3D structures are expected to have the same specific surface area defined by (Yeong and Torquato, 1998a)

$$s = -6\left(\phi - \phi^2\right)\left.\frac{\mathrm{d}R_z(u)}{\mathrm{d}u}\right|_{u=0} \tag{6}$$

The specific surface area calculated from the measured microstructure is 0.122 for Fontainebleau, 0.188 for Berea sandstone, while the calculated average values for the reconstructed media are 0.145 and 0.191, respectively. The slightly higher values in the reconstructed images are due to noise

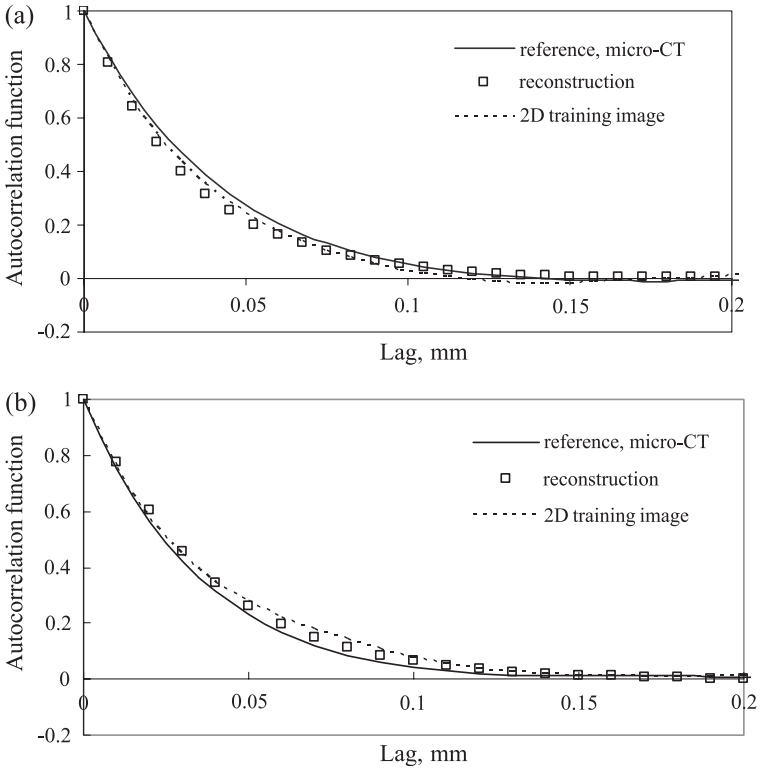

Fig. 16. Void–void autocorrelation functions of the sandstones studied averaged over three principal orthogonal axes. (a) Fontainebleau sandstone. (b) Berea sandstone. The results of the reconstructed structures are compared with those of the microstructure measured by micro-CT and those of training images.

in the image generated by the multiple-point statistics reconstruction.

4.5. Fraction of percolating cells in the reconstructed microstructure

A key aspect of the reconstruction is the possibility of reproducing long-range connectivity. For multiple-point reconstruction on Fontainebleau sandstone, 8% of the void space in the reconstructed structure is not connected to the main pore phase cluster compared to 2% in the reference structure. This is principally due to noise in the image. However, visual inspection of structures does not reveal the degree of connectivity. Traditional characteristics such as porosity, specific surface area and two-point correlation functions are also insufficient to distinguish different microstructures because they are all low-order information and relatively easy to reproduce. A quantitative characterization of the connectivity is provided by the local percolation probabilities or fraction of percolating cells defined by

$$p_3(L) = \frac{1}{m} \sum_r \Lambda_3(r, L) \tag{7}$$

where m is the number of measurement and $\Lambda_3(r,L)$ is an indicator of percolation (Hilfer, 2002).

$$\Lambda_3(r, L) = \begin{cases} 1 & \text{if } M(r, L) \text{ percolates 3 directions} \\ 0 & \text{otherwise} \end{cases} \tag{8}$$

A measurement cube $M(\mathbf{r}, L)$ of sidelength L centered at position $\mathbf{r}$ is used to calculate the condition of continuous connectedness from one face to opposite face by percolation theory (Stauffer and Aharony, 1994). In 3D discretized media, 26 nearest neighbors are used to measure the pore connectedness. This property shows considerable difference between different reconstruction approaches. Figs. 17 and 18 show the reproduction of long-range con-

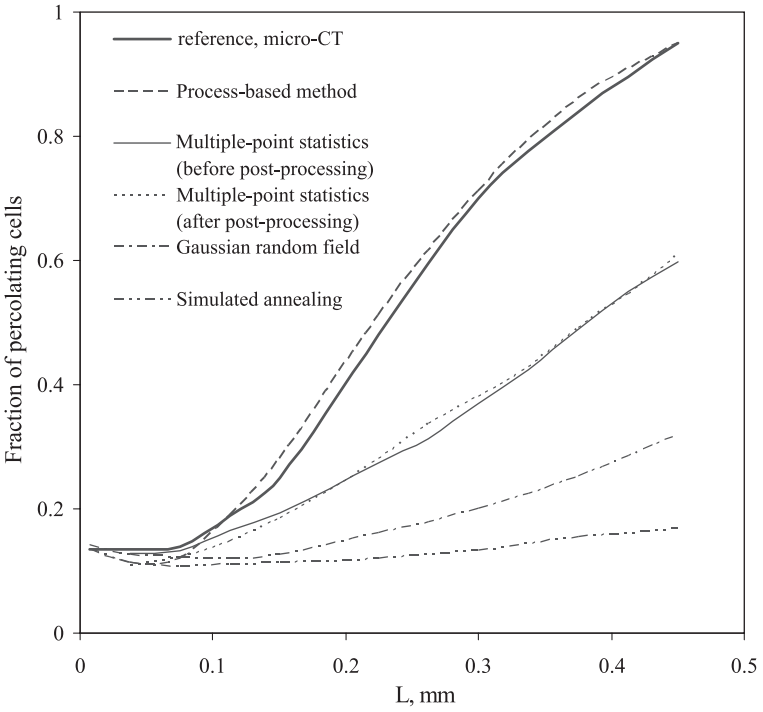

Fig. 17. Fraction of percolating cells for Fontainebleau sandstone images using different reconstruction methods. Notice that incorporating higher-order information in the reconstruction significantly improves the long-range connectivity of the pore space, although it still performs less well than process-based reconstruction methods. The data except multiple-point statistics and micro-CT are taken from (Biswal et al., 1999).

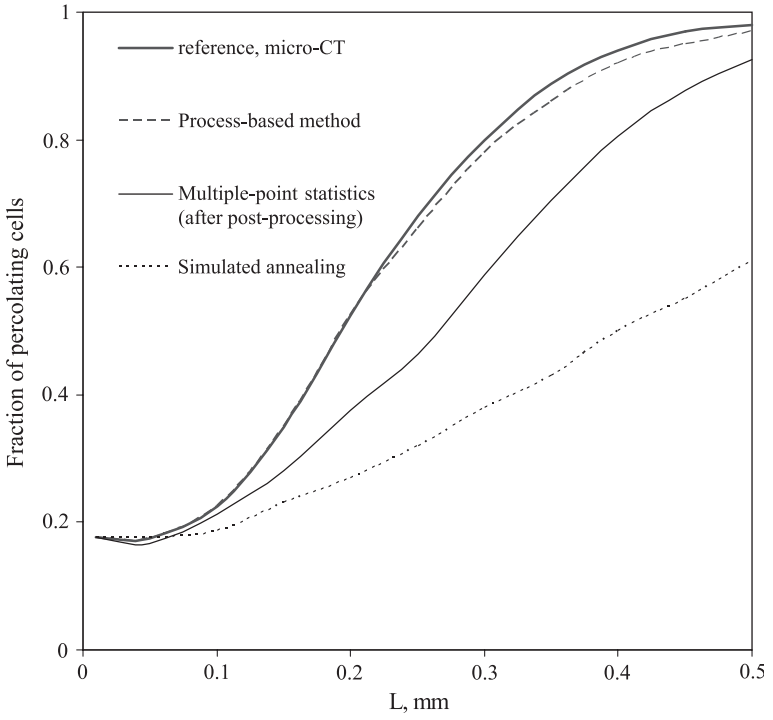

Fig. 18. Fraction of percolating cells for Berea sandstone images using different reconstruction methods. Notice that incorporating higher-order information in the reconstruction significantly improves the long-range connectivity of the pore space, although it still performs less well than process-based reconstruction methods. The data except multiple-point statistics and micro-CT are taken from (Øren and Bakke, 2003).

nectivity. The post-processing does not change the fraction of percolating cells. The results shown are averages over ten unconditional and conditional realizations. However, each individual realization gave results very similar to the average. The figures also plot the fraction of percolating cells for reconstructions using a low-order statistics method, the Gaussian random field method and/or simulated annealing, which matched traditional low-order properties such as porosity and two-point correlation functions (Biswal et al., 1999; Øren and Bakke, 2003). The results are also compared to process-based reconstruction by Øren and Bakke (2002, 2003). In these figures the reference measured by micro-CT and the process-based method give similar results but differ from those for the structure generated using stochastic reconstructions. The figures also show that reconstruction methods based on low-order correlation functions fail to reproduce the long-range connectivity of porous media, while the process-based method successfully reproduces the connectivity. Our multiple-point statistics method significantly improves the connectivity over the two-point statistics methods for both sandstones, although the pore space is still less well connected than the reference image, especially for low porosity Fontainebleau sandstone.

5. Conclusions

A multiple-point statistics methodology using 2D thin sections to generate 3D pore-space representations of rocks was validated in this paper. Fontainebleau and Berea sandstones were used for the study because their pore size is large enough to be captured by microtomography to provide reference datasets. Visual inspection of the images and the measurement of the fraction of percolating cells have confirmed the ability of the method to reproduce long-range connectivity, which is difficult to achieve using traditional two-point statistics reconstructions. Isotropy is assumed in the reconstruction; however, more

conditioning data, such as several thin section images, can be used as constraints and multi-orientation thin section images can provide more statistics when anisotropy is expected. Process-based reconstruction is promising if the detailed geological history is available. On the other hand the multiple-point statistics method is more general and it can generate realistic pore space images without knowledge of geological processes by which the rock was formed. The method, therefore, is suitable for rocks with complex geological history and abundant sub-micron pores, such as many carbonates, that cannot be characterized so far by direct measurement, such as micro-CT scanning.

Nomenclature

$c(\text{dev}_n)$ replicate of dev_n found in a training image
dev data event (or pattern)
$\mathbf{h}_\alpha$ vector describing a template
$i(\mathbf{u})$ data value at $\mathbf{u}$ in a template
m number of measurement
$M(\boldsymbol{r}, L)$ measurement cube of sidelength L centered at position $\mathbf{r}$
n_t number of location in a *template t* (= size of a *template t*)
N_n size of a training image
N_t number of different central locations of a *template t*
$\mathbf{u}$ central location in a template
$\mathbf{u}_\alpha$ location in a template
$p_3(L)$ local percolation probability
$\Pr(\text{dev}_n)$ proportion of multiple-point statistics
$\vec{r}$ vector describing microstructure
$R_Z(\vec{u})$ void–void autocorrelation function
s specific surface area calculated using autocorrelation function
Set training data set constructed with a template
$\vec{u}$ lag vector
$Z(\vec{r})$ binary phase function
$\Lambda_3(r,L)$ indicator of percolation.

Acknowledgements

The authors express their gratitude to all the members of the Imperial College consortium on Pore-Scale Modeling (BHP, Enterprise Oil, Gaz de France, JNOC, PDVSA-Intevep, Schlumberger, Shell, Statoil and the U.K. Department of Trade and Industry) for financial and technical support of our research. We thank David Stern (ExxonMobil) and Pål-Eric Øren (Statoil) for sharing the experimental data set with us.

References

Adler, P.M., Jacquin, C.G., Quiblier, J.A., 1990. Flow in simulated porous-media. International Journal of Multiphase Flow 16 (4), 691–712.

Adler, P.M., Jacquin, C.G., Thovert, J.F., 1992. The formation factor of reconstructed porous-media. Water Resources Research 28 (6), 1571–1576.

Bakke, S., Øren, P.E., 1997. 3-D pore-scale modelling of sandstones and flow simulations in the pore networks. SPE Journal 2 (2), 136–149.

Biswal, B., Manwart, C., Hilfer, R., Bakke, S., Øren, P.E., 1999. Quantitative analysis of experimental and synthetic microstructures for sedimentary rock. Physica A 273 (3–4), 452–475.

Blunt, M.J., Jackson, M.D., Piri, M., Valvatne, P.H., 2002. Detailed physics, predictive capabilities and macroscopic consequences for pore-network models of multiphase flow. Advances in Water Resources 25 (8–12), 1069–1089.

Bourbie, T., Coussy, O., Zinszner, B., 1987. Acoustics of Porous Media. Gulf Publishing Company, Paris.

Bryant, S., Blunt, M., 1992. Prediction of relative permeability in simple porous-media. Physical Review A 46 (4), 2004–2011.

Caers, J., 2001. Geostatistical reservoir modelling using statistical pattern recognition. Journal of Petroleum Science and Engineering 29 (3–4), 177–188.

Chen, S., Doolen, G.D., 1998. Lattice Boltzmann method for fluid flows. Annual Review of Fluid Mechanics 30, 329–364.

Coles, M.E., et al., 1998. Developments in synchrotron X-ray microtomography with applications to flow in porous media. SPE Reservoir Evaluation and Engineering 1 (4), 288–296.

Dullien, F.A.L., 1992. Porous Media: Fluid Transport and Pore Structure. Academic Press, San Diego.

Dunsmuir, J.H., Ferguson, S.R., D'Amico, K.L., Stokes, J.P., 1991. X-ray microtomography. A new tool for the characterization of porous media, SPE 22860. Proc. Annual Technical Conference, Dallas, Texas, October 6–9, 1991, pp. 423–430.

Fredrich, J.T., 1999. 3D imaging of porous media using laser scanning confocal microscopy with application to microscale transport processes. Physics and Chemistry of the Earth. Part A: Solid Earth and Geodesy 24 (7), 551–561.

Hazlett, R.D., 1995. Simulation of capillary-dominated displacements in microtomographic images of reservoir rocks. Transport in Porous Media 20 (1–2), 21–35.

Hazlett, R.D., 1997. Statistical characterization and stochastic modeling of pore networks in relation to fluid flow. Mathematical Geology 29 (6), 801–822.

Hilfer, R., 2002. Review on scale dependent characterization of the microstructure of porous media. Transport in Porous Media 46 (2–3), 373–390.

Ioannidis, M.A., Kwiecien, M.J., Chatzis, I., 1997. Electrical conductivity and percolation aspects of statistically homogeneous porous media. Transport in Porous Media 29 (1), 61–83.

Kainourgiakis, M.E., et al., 2000. Structural and transport properties of alumina porous membranes from process-based and statistical reconstruction techniques. Journal of Colloid and Interface Science 231 (1), 158–167.

Levitz, P., 1998. Off-lattice reconstruction of porous media: critical evaluation, geometrical confinement and molecular transport. Advances in Colloid and Interface Science 77, 71–106.

Liang, Z.R., Fernandes, C.P., Magnani, F.S., Philippi, P.C., 1998. A reconstruction technique for three-dimensional porous media using image analysis and Fourier transforms. Journal of Petroleum Science and Engineering 21 (3–4), 273–283.

Lindquist, W.B., Venkatarangan, A., Dunsmuir, J., Wong, T.F., 2000. Pore and throat size distributions measured from synchrotron X-ray tomographic images of Fontainebleau sandstones. Journal of Geophysical Research, [Solid Earth] 105 (B9), 21509–21527.

Lucia, F.J., 1999. Carbonate Reservoir Characterization. Springer, Berlin, Germany.

Manwart, C., Torquato, S., Hilfer, R., 2000. Stochastic reconstruction of sandstones. Physical Review E 62 (1), 893–899.

Øren, P.E., Bakke, S., 2002. Process based reconstruction of sandstones and prediction of transport properties. Transport in Porous Media 46 (2–3), 311–343.

Øren, P.E., Bakke, S., 2003. Reconstruction of Berea sandstone and pore-scale modelling of wettability effects. Journal of Petroleum Science and Engineering 39 (3–4), 177–199.

Pilotti, M., 2000. Reconstruction of clastic porous media. Transport in Porous Media 41 (3), 359–364.

Quiblier, J.A., 1984. A new three-dimensional modeling technique for studying porous-media. Journal of Colloid and Interface Science 98 (1), 84–102.

Roberts, A.P., 1997. Statistical reconstruction of three-dimensional porous media from two-dimensional images. Physical Review E 56 (3), 3203–3212.

Roberts, A.P., Torquato, S., 1999. Chord-distribution functions of three-dimensional random media: approximate first-passage times of Gaussian processes. Physical Review E 59 (5), 4953–4963.

Russ, J.C., 1994. The Image Processing Handbook, 2nd edition. CRC Press, Boca Raton, Florida.

Serra, J., 1992. Image Analysis and Mathematical Morphology. Academic Press, New York.

Spanne, P., et al., 1994. Synchrotron computed microtomography of porous-media-topology and transports. Physical Review Letters 73 (14), 2001–2004.

Stauffer, D., Aharony, A., 1994. Introduction to Percolation Theory, 2nd ed. Taylor and Francis, London and New York.

Strebelle, S., Payrazyan, K., Caers, J., 2003. Modeling of a deepwater turbidite reservoir conditional to seismic data using principal component analysis and multiple-point geostatistics. SPE Journal 8 (3), 227–235.

Talukdar, M.S., Torsaeter, O., Ioannidis, M.A., 2002. Stochastic reconstruction of particulate media from two-dimensional images. Journal of Colloid and Interface Science 248 (2), 419–428.

Tomutsa, L., Radmilovic, V., 2003. Focussed ion beam assisted three-dimensional rock imaging at submicron-scale. International Symposium of the Society of Core Analysts: SCA2003-47.

Yeong, C.L.Y., Torquato, S., 1998a. Reconstructing random media. Physical Review E 57 (1), 495–506.

Yeong, C.L.Y., Torquato, S., 1998b. Reconstructing random media: II. Three-dimensional media from two-dimensional cuts. Physical Review E 58 (1), 224–233.